High Power Laser Science and Engineering, (2024), Vol. 12, e53, 10 pages.
doi:10.1017/hpl.2024.29

HIGH POWER LASER SCIENCE AND ENGINEERING

RESEARCH ARTICLE

In-vacuum post-compression of optical probe pulses for relativistic plasma diagnostics

S. Lorenz[1,2], G. M. Grittani[1], K. Kondo[3], A. Kon[3], Y.-K. Liu[4], A. Sagisaka[3], K. Ogura[3], N. Nakanii[3], K. Huang[3], A. Bierwage[5,6], S. Namba[7], H. Ohiro[7], T. A. Pikuz[8], J. K. Koga[3], P. Chen[4], H. Kiriyama[3], M. Kando[3], T. Zh. Esirkepov[3], S. V. Bulanov[1,3], and A. S. Pirozhkov[3]

[1] *Extreme Light Infrastructure ERIC, ELI Beamlines Facility, Dolni Brezany, Czech Republic*

[2] *Czech Technical University in Prague, FNSPE, Prague, Czech Republic*

[3] *Kansai Institute for Photon Science, National Institutes for Quantum Science and Technology, Kyoto, Japan*

[4] *Leung Center for Cosmology and Particle Astrophysics, National Taiwan University, Taipei, Taiwan*

[5] *Rokkasho Fusion Institute, National Institutes for Quantum Science and Technology, Aomori, Japan*

[6] *Naka Fusion Institute, National Institutes for Quantum Science and Technology, Ibaraki, Japan*

[7] *Department of Advanced Science and Engineering, Hiroshima University, Hiroshima, Japan*

[8] *Institute for Open and Transdisciplinary Research Initiatives, Osaka University, Osaka, Japan*

(Received 3 January 2024; revised 20 April 2024; accepted 6 May 2024)

Abstract

Ultrafast optical probing is a widely used method of underdense plasma diagnostic. In relativistic plasma, the motion blur limits spatial resolution in the direction of motion. For many high-power lasers the initial pulse duration of 30–50 fs results in a 10–15 μm motion blur, which can be reduced by probe pulse post-compression. Here we used the compression after compressor approach [Phys.-Usp. **62**, 1096 (2019); JINST **17** P07035 (2022)], where spectral broadening is performed in thin optical plates and is followed by reflections from negative-dispersion mirrors. Our initially low-intensity probe beam was down-collimated for a more efficient spectral broadening and higher probe-to-self-emission intensity ratio. The setup is compact, fits in a vacuum chamber and can be implemented within a short experimental time slot. We proved that the compressed pulse retained the high quality necessary for plasma probing.

Keywords: compression after compressor approach; probe pulse post-compression; relativistic plasma imaging; ultrafast optical probing

1. Introduction

In laser–plasma experiments, a fraction of the driving laser pulse is typically used as an ultrafast probe of the interaction process. This is advantageous due to the minimization of jitter between the two pulses. Successful implementation of this technique enables the observation of wake waves in a plasma behind the laser driver[1–3], injection dynamics[4,5] and magnetic field structures[6] in the electron acceleration process[7]. Significantly interesting is the optical probing of electron density singularities of a relativistic plasma[8] capable of reflecting light via the double Doppler effect in the relativistic flying mirror mechanism[9–12] or emitting bright coherent soft-X-ray radiation in the course of burst intensification by singularity emitting radiation (BISER)[13–18]. However, images of sharply localized relativistic singularities obtained by means of ultra-short probe pulses with duration τ are blurred to sizes of approximately $c\tau$ due to the motion blur, where c is the speed of light. For 30–50 fs probe pulse durations, typical for high-power femtosecond lasers, this blurring reduces the spatial resolution to approximately 10−15 μm, which is often insufficient. The blurring effect can be reduced by compressing the probe pulse after the pick-off from the main pulse (post-compression)[19], which is a complicated technical task, taking into consideration that the femtosecond synchronization level should be retained.

Post-compression of the probe pulse is performed in two distinct steps: spectral broadening induced by

Correspondence to: S. Lorenz, Extreme Light Infrastructure ERIC, ELI Beamlines Facility, Za Radnici 835, 25241 Dolni Brezany, Czech Republic. Email: sebastian.lorenz@eli-beams.eu; A. S. Pirozhkov, Kansai Institute for Photon Science, National Institutes for Quantum Science and Technology, 8-1-7 Umemidai, Kizugawa-city, Kyoto 619-0215, Japan. Email: pirozhkov.alexander@qst.go.jp

time-dependent self-phase modulation (SPM) driven by the optical Kerr effect[20,21] followed by chirp compensation with the use of a set of chirped mirrors[22–24]. Two methods can be used for compression of the probe pulses: spectrum broadening achieved either in a gas-filled hollow fiber[25,26] or in a solid nonlinear medium (e.g., thin glass, crystal or plastic plates[27–30]) proposed originally as thin film compression by Prof. G. Mourou *et al.*[31] in 2014. The method implementing a solid nonlinear medium for SPM after the main laser compressor is called the compression after compressor approach (CafCA)[32–34]. Gases have very small nonlinearity coefficients, thus requiring intense focused pulses propagating through long (tens of cm or even meters) fibers to achieve significant SPM-induced spectral broadening. On the other hand, solid nonlinear media of the CafCA have much higher nonlinearities, thus operating at much lower intensities and with thin (millimeter-scale) plates. In both cases, the broad-bandwidth pulse after the SPM is compressed by negative-dispersion mirrors to durations several times shorter than the original laser pulse.

Up to now most post-compressed probe experiments were performed using SPM in gas-filled hollow fibers, for example[4,35]. However, this usually requires bringing the probe out of the main vacuum beamline, using a few-meter-long compression beamline including a gas-filled hollow fiber and a long-focal-length lens or mirror and bringing the compressed probe back into the interaction vacuum chamber[36]. In contrast, the CafCA uses a shorter beamline and can be implemented in-vacuum, which significantly simplifies the setup and reduces the main-to-probe pulse jitter. Because of its compactness, the alignment is time effective and the whole CafCA setup can be built on an insertable stage, and therefore the post-compression can be switched on/off online during an experiment. On the other hand, the following challenges arise during the high-power laser plasma experiments.

Reaching sufficient probe beam peak intensity for efficient SPM in thin plates. In order to minimize the temporal jitter between the main pulse and the probe, the latter has to be taken from the former either by wave front splitting, by the leakage of one reflective component or by taking the edge of the main pulse with a pick-off mirror. These processes lead to probe beams with peak intensity significantly lower than the main laser pulse, so that SPM in thin plates becomes inefficient and cannot provide significant spectrum broadening. This can be overcome by focusing the probe pulse or its down-collimation before SPM; however, this is not a trivial task, taking into account the fact that the setup should be compact and the temporal and spatial beam qualities should be preserved to a high degree. Alternatively, the SPM can be increased by increasing the nonlinear medium thickness, but this induces greater material dispersion, which is also positive and thus requires a larger number of bounces from the negative-dispersion mirrors, which complicates the in-vacuum setup.

Shot-to-shot peak intensity variations leading to compressed probe duration fluctuations. The near-field peak intensity distribution of high-power laser systems exhibits some variations, especially at the beam edges, which are often used for probe pick-off mirror locations. Such variations will directly translate into SPM variation and therefore to compressed probe duration fluctuations.

Compressed probe duration dependence on the main pulse energy. It is typical for high-power laser experiments to scan the main pulse energy to study dependences of various processes of interest on the laser power or intensity. The probe pulse, split from the main one near the interaction point, will have its peak intensity proportional to the main pulse energy. Thus, the SPM will be affected, and therefore the compressed probe duration as well.

Potential degradation of the probe pulse near-field pattern. SPM is a nonlinear process and for large B-integrals can cause filamentation. Even if not reaching this extreme case, the wavefront quality, and therefore after propagation the near-field pattern, can be degraded. Further, the probe beam focusing or down-collimation discussed above can influence the near-field quality as well. These processes can affect the quality of the optical shadowgrams, interferometry and Schlieren images.

Typically short experimental beam times of high-power user facilities. Policies of high-power laser facilities vary, but it is typical to grant from 1 to 6 weeks for a single experimental proposal. During this time, the team should build and optimize the entire setup (not only the probe line). This issue can be overcome by preparing the compressed probe line in advance as a part of the facility work, but this option is not always possible.

Since we did not intentionally change the initial (before post-compression stage) pulse duration, and it was almost constant in all laser modes we used, we can assume that the beam fluence and pulse peak intensity are strongly correlated. We will be using both of these quantities in the following text.

Our work is aimed at shortening probe pulses using the CafCA[33] based on nonlinear spectrum broadening in optical plates followed by post-compression of the pulse by chirped mirrors, and testing how the above issues affect real experiments. We show experimental results where an initially low-fluence, approximately $1-10\ \mathrm{mJ/cm^2}$ 50 fs, probe beam was down-collimated to achieve a fluence of approximately $100-1000\ \mathrm{mJ/cm^2}$, and compressed down to approximately 20 fs, which reduced the motion blurring effect in the probe images by the factor of 2.5. We used the setup for probing relativistic underdense plasma (1 mm diameter conical gas jet with electron density from $\sim 2\times 10^{19}$ to $> 10^{20}\ \mathrm{cm^{-3}}$,

characteristic for BISER experiments) in the shadow and Schlieren modes. We also characterized shot-to-shot probe duration fluctuations and the dependence of the probe duration and its statistical properties on the main pulse energy. We found the optimum main pulse energy for which the probe duration fluctuations were minimized.

2. Experimental setup

The experiment was carried out with the J-KAREN-P laser system[37,38] as part of a standard 4-week beam time with additional 4 weeks for setup. The experimental setup is shown in Figure 1. The probe beam was extracted by inserting a flat elliptical 45° incidence 1" pick-off mirror off to the side of the main laser beam (∼11 inch diameter). The measured probe beam fluence was approximately $1-10\ \mathrm{mJ/cm^2}$ (depending on the main pulse energy), and the time duration of the driver laser was 50 fs measured by self-referenced spectral interferometry[39] with a commercial Wizzler device (Wizzler I in Figure 1). In order to achieve efficient spectral broadening, the probe beam was down-collimated 10.7 times by an $f = 750$ mm achromatic doublet lens and an $f = 70$ mm singlet lens. Transmissive optics has been used in order to keep the original probe line path, which was necessary due to the limited delay stage range (a reflective down-collimation option would elongate delay beyond the available range, which would require complete rebuilding of the probe line). The configuration was an experimental trade-off between increasing the fluence of the probe pulse and keeping its pointing stability to a level sufficient to maintain the spatial alignment with the main (driver) laser, which becomes increasingly sensitive as the down-collimation ratio increases. Nevertheless, the singlet lens was mounted on a three-axis motorized stage to adjust its position to a few μm level to fine-tune its alignment. Without this motorization, the alignment shift of the probe beam due to target chamber pumping led to complete loss of the probe image. A significant additional benefit from the down-collimation was increased probe pulse fluence, which helped one to see the probe despite the very bright plasma self-emission – we note that in contrast to electron acceleration[40,41], the BISER experiments require relatively high plasma density of typically a few times $10^{19}\ \mathrm{cm^{-3}}$ up to more than $10^{20}\ \mathrm{cm^{-3}}$, relatively high intensity ($> 10^{20}\ \mathrm{W/cm^2}$ after self-focusing) and high probe magnification, which make the plasma self-emission one of the most important experimental challenges. High plasma densities are advantageous also for bright betatron radiation[42].

The compactness of the CafCA setup allowed building the entire post-compressor on an insertable breadboard moved by a 300 mm in-vacuum translation stage, which allowed using the compressed or the original probe pulses, whereas the relatively small delay difference was compensated by a 300 mm delay line stage. When ultra-short broadband laser

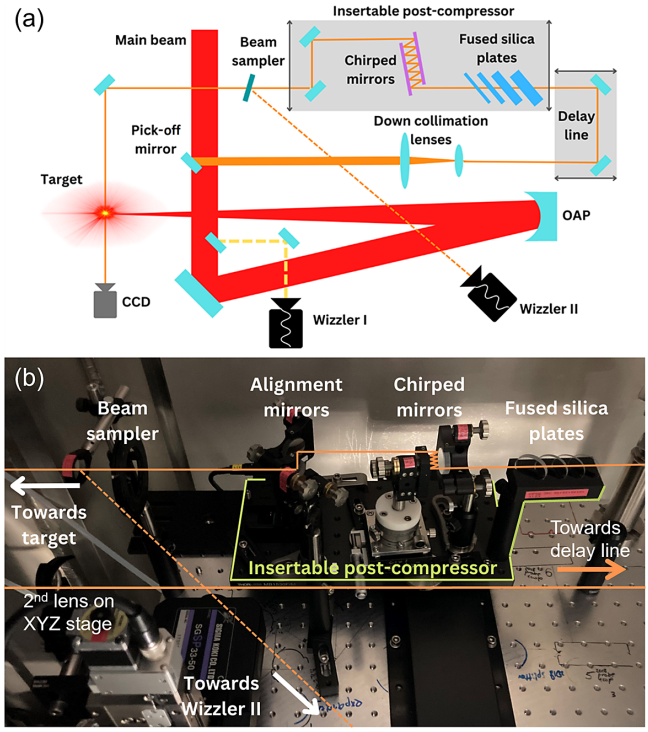

Figure 1. (a) Scheme of the compressed probe setup and (b) labeled image of the post-compressor station.

pulses propagate through transmissive optics, three main effects have to be taken into account: firstly, each wavelength propagates at a different speed inside the media, resulting in an increased group delay dispersion (GDD) of the laser pulse; secondly, owing to the difference between the phase and group velocity, the pulse front may be delayed with respect to the phase front[43,44]; thirdly, the transmissive optical element can be affected as the laser fluence approaches the damage threshold.

The GDD can be estimated by knowing the material-specific group velocity dispersion (GVD), the lens thickness and the laser wavelength. The pulse front delay can be expressed by the following equation[44]:

$$\mathrm{PTD} = \frac{r^2}{2cf\,(n-1)}\left(-\lambda\frac{\mathrm{d}n}{\mathrm{d}\lambda}\right), \tag{1}$$

where PTD is the propagation time difference, r is the probe beam radius, λ is the laser wavelength, n is the refractive index of the lens material and f is the focal length of the lens. It can be expressed also in typical experimental units as follows:

$$\mathrm{PTD\,[fs]} \simeq 1.7\times10^{3}\times\frac{r\,[\mathrm{mm}]^2}{f\,[\mathrm{mm}]}\times\frac{\lambda\,[\mu\mathrm{m}]}{n-1}\times\left(-\frac{\mathrm{d}n}{\mathrm{d}\lambda}\left[\mu\mathrm{m}^{-1}\right]\right). \tag{2}$$

The GDD can be compensated by negative-dispersion mirrors, while the PTD compensation is non-trivial.

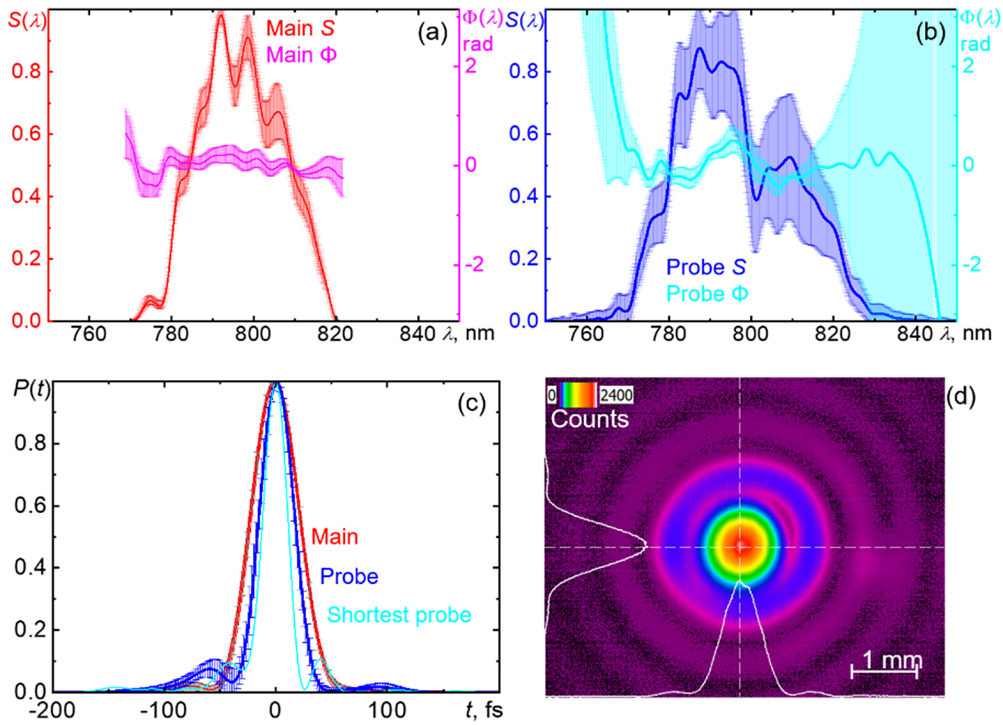

Figure 2. Main and probe pulses before the experiment. (a)–(c) Power amplifier (PA) mode, 1000-shot average for the main and probe pulses, where the error bars are standard deviations of shot-to-shot variations. (a) Red is the main pulse spectrum, while magenta is the main pulse spectral phase. (b) Blue is the probe pulse spectrum, while cyan is probe pulse spectral phase. (c) Red and blue are the main and probe pulse shapes, while cyan is the shortest probe pulse. (d) Down-collimated probe beam spatial profile measured before the fused silica plates by using a low-power infrared laser diode alignment beam.

By taking these three effects into consideration, the first lens of the down-collimating system was chosen to be a 6.7 mm thick achromatic doublet, and the second lens was chosen as a 3.4 mm thick singlet lens. The first lens, being achromatic, did not add pulse front delay, but at the same time added 738 fs^2 GDD to the probe pulse. The second lens added a negligible 0.7 fs pulse front delay and 149 fs^2 GDD. The down-collimated probe beam spatial profile measured after the down-collimation before the fused silica (FS) plates is plotted in Figure 2(d). This spatial profile was measured by using a low-power infrared laser diode alignment beam that had been aligned to match the size (280 mm), divergence and near field and far field of the main Ti:sapphire laser beam[37], and an insertable complementary metal–oxide–semiconductor (CMOS) camera. The on-shot probe pulse profile is shown in the Supplementary Materials (Figure S3).

After propagating through the two lenses, the laser pulse achieved a fluence of approximately 100−1000 mJ/cm^2 (depending on the pulse energy), which was sufficient to drive the nonlinear processes required to achieve spectral broadening within a few mm of FS[34]. The laser pulse propagated through a sequence of 1, 2, 3 and 5 mm thick, plane-parallel FS plates set at the Brewster's angle (angle of incidence 55.6°), which created a 14 mm long beam path inside the FS material. After that, the laser pulse was compressed by broad-band dispersive mirrors (chirped mirrors) with a nominal GDD of –40 fs^2 and incidence angle of 5° (model PC5 from Ultrafast Innovations). This post-compressed pulse was used for the plasma probing, while its small fraction was split with an ultrafast beam sampler and sent to the second Wizzler device (Wizzler II in Figure 1) for simultaneous pulse shape measurement. We used an identical beam sampler in transmission in front of Wizzler II for the compensation of the main beam sampler effect on the probe. We also post-processed the Wizzler II results, subtracting the dispersion of the 2 mm thick CaF_2 window and air.

3. Results

Figures 2(a)–2(c) show measurements in the power amplifier (PA) mode at 10 Hz carried out before the main experiment. Fluctuations of the probe spectrum were not symmetric: the red part contained larger shot-to-shot fluctuations (Figure 2(b)), which can be explained by the main pulse statistical properties (Supplementary Materials, Figure S2). The main pulse had the full width at half maximum (FWHM) duration $\tau_{FWHM} = 48.6 \pm 0.8$ fs (transform limit $\tau_{TL} = 48.0$ fs) and effective width $\tau_{Eff} = 52.0 \pm 1.6$ fs, while the compressed probe had $\tau_{FWHM} = 36 \pm 3$ fs ($\tau_{TL} = 31$ fs) and $\tau_{Eff} = 42 \pm 3$ fs. Here the effective width is the area under the normalized power curve: $\tau_{Eff} = \int p(t)dt$, where $p(t) = P(t)/P_{max}$[37].

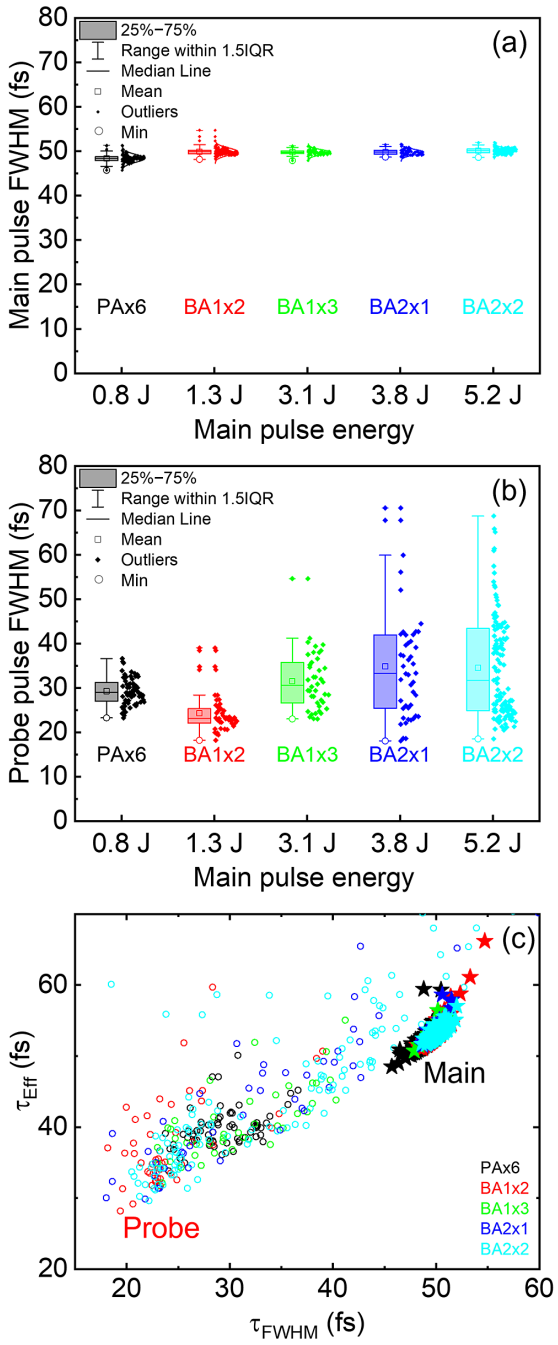

Figure 3. On-shot main and probe pulse measurements during one experimental day in several laser modes. The box-and-whisker plots of the main pulse (a) and probe pulse (b) FWHM durations versus the laser mode and main pulse energy. The colored bars represent the 25%–75% ranges, the error bars are the 1.5 interquartile ranges, the horizontal lines are the medians and the squares, dots and circles are the means, outliers and minima, respectively. The dots on the right from the boxes-and-whiskers are the individual shots forming the corresponding histograms. (c) Main (stars) and probe (rings) pulses on the [FWHM, effective pulse width] plane; each point is an individual shot. Color encodes the laser mode.

Figure 3 shows measurements of the main and compressed probe pulses during the experiment in several laser modes, that is, PA with approximately 15 TW on target and booster amplifiers 1 and 2 (BA1 and BA2) with up to 100 TW. The ×1, ×2, etc., labels denote (partial) pumping levels of each amplifier used to control the pulse energy, which are shown as abscissas in the Figures 3(a) and 3(b); a more detailed description is provided in Ref. [45]. The main pulse duration remained nearly the same in all the laser modes. On the other hand, the probe's SPM gradually increased with the laser energy, while the negative dispersion provided by the chirped mirrors remained constant. In this configuration, the probe pulse compression was achieved in the majority of the laser shots. On the other hand, the stability of the compressed probe pulse duration was not as high as the initial pulse. We attribute this to the pulse-to-pulse fluence variation at the edge of the main beam, where the pick-off mirror was placed. In our setup (14 reflections from the chirped mirrors), the optimum compression and the highest stability were achieved in the BA1×2 mode, but the minimum probe duration was approximately 18−20 fs in all laser modes with the main pulse energy larger than 1 J. In the PA and BA1×3 modes, the average probe duration was somewhat larger. At higher energies (BA2×1, BA2×2 modes), the compressed probe had even larger average duration and lower stability. The compressed probe was longer than its transform limit due to the remaining chirp and higher-order phase terms, especially in the higher-energy modes. In the optimum BA1×2 mode, we obtained $\tau_{FWHM} = 24 \pm 5$ fs (without outliers, $\tau_{FWHM} = 23 \pm 2$ fs) with the transform limit $\tau_{TL} = 22 \pm 6$ fs, and $\tau_{Eff} = 38 \pm 6$ fs. The histogram in Figure 4(a) shows that the most frequent probe duration in this optimum mode was 23 fs with a few outliers up to 40 fs. Nevertheless, the shortest probe pulses were compressed down to $\tau_{FWHM} = 18$ fs and $\tau_{Eff} = 30$ fs (Figure 4(b)). For this pulse shape with relatively few low-intensity satellite pulses, the main parameter determining resolution is the FWHM[19,34]; thus, the temporal blur with this probe pulse was reduced approximately 2.6 times compared to the original best 46 fs probe duration.

Furthermore, analysis of the influence of probe energy fluctuation was performed (Figure 5). As the probe energy was not measured on-shot, we used the measured main pulse on-shot near-field profile to estimate probe energy within 1" apertures near the actual probe (Supplementary Materials, Figure S1). Figure 5(a) shows fluctuation of probe energy estimated in this way, compared to the same fluctuation for the 1" aperture at the main beam center. The relative probe energy fluctuation reached up to the value of 0.38 at the highest energies. Dependence of the probe duration (FWHM) on the estimated probe energy is displayed in Figures 5(b) and 5(c). There was a strong correlation observed at low pulse energies, where the compression was nearly perfect (compared with the ideal compression estimated using Refs. [33,34], open circles). At higher energies, there was a complex dependence due to interplay of probe energy fluctuation and imperfect compression.

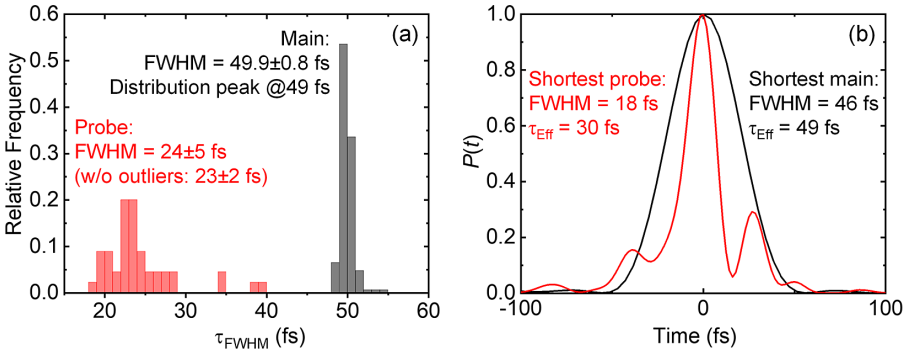

Figure 4. Stability of the probe pulse compression and the shortest measured pulses. (a) FWHM histograms for the BA1×2 mode, which provides the optimum average compression. (b) Shortest main and probe pulses; the latter was obtained in the BA2×1 laser shot with the main pulse energy of 4 J and probe pulse energy of approximately 5.8 mJ.

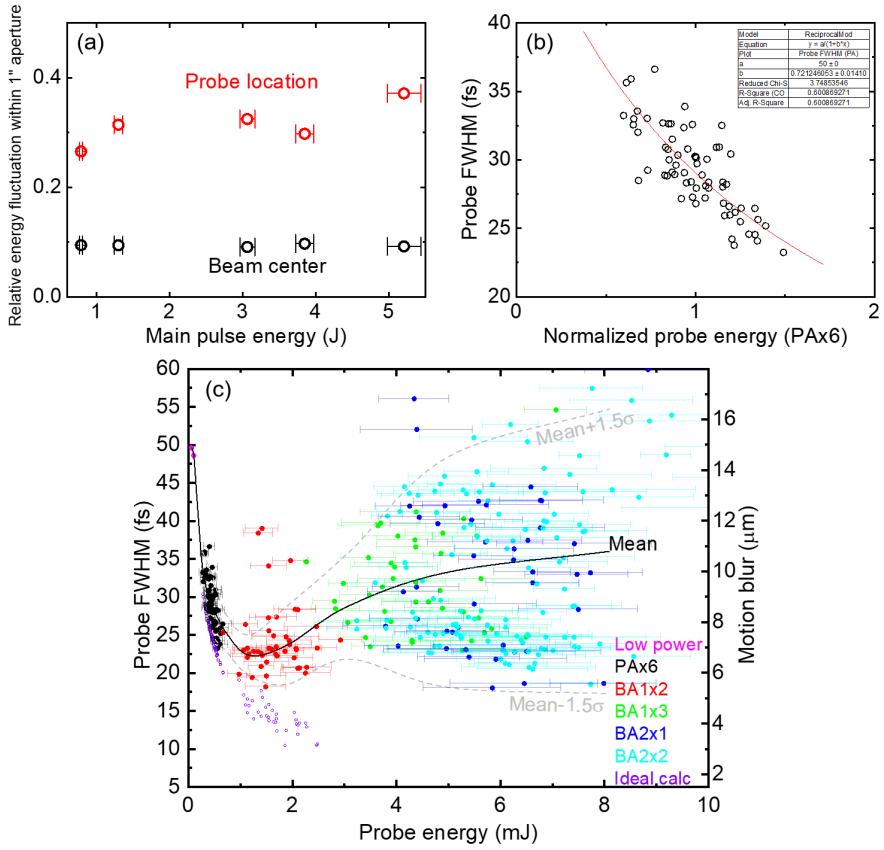

Figure 5. Analysis of the dependence of probe pulse duration on the probe and main pulse energy. (a) Relative energy fluctuation (standard deviation divided by mean) in 1" apertures near the edge of the main beam (approximately probe location, red) and at the center of the main beam (black) in different laser modes. (b) Probe pulse duration dependence on the estimated probe energy in the PA×6 laser mode. The red line is a one-parameter fit corresponding to Equation (11b) of Ref. [33]. (c) Probe pulse duration dependence on the estimated probe energy for all studied laser modes (solid circles) and estimated[33,34] probe duration assuming ideal compression (open circles); the right-hand axis shows the motion blur.

Figure 6 shows representative images of the relativistic plasma obtained with the original (Figure 6(a)) and down-collimated compressed probe in the shadow (Figure 6(b)) and Schlieren (Figures 6(c) and 6(d)) modes. Each image captures a different shot with similar laser and target parameters. In all images, a time-integrated self-emission can be observed, accumulated during the entire camera exposure time. On the other hand, the ultra-short snapshots of the plasma channel were acquired by the femtosecond probe pulse. In contrast to the original probe (Figure 6(a)), where the probe-produced image was barely visible on top of the bright self-emission, the down-collimated compressed probe was clearly visible, although the self-emission was still present.

Further, the images demonstrate that despite the down-collimation and nonlinear process (SPM), the probe

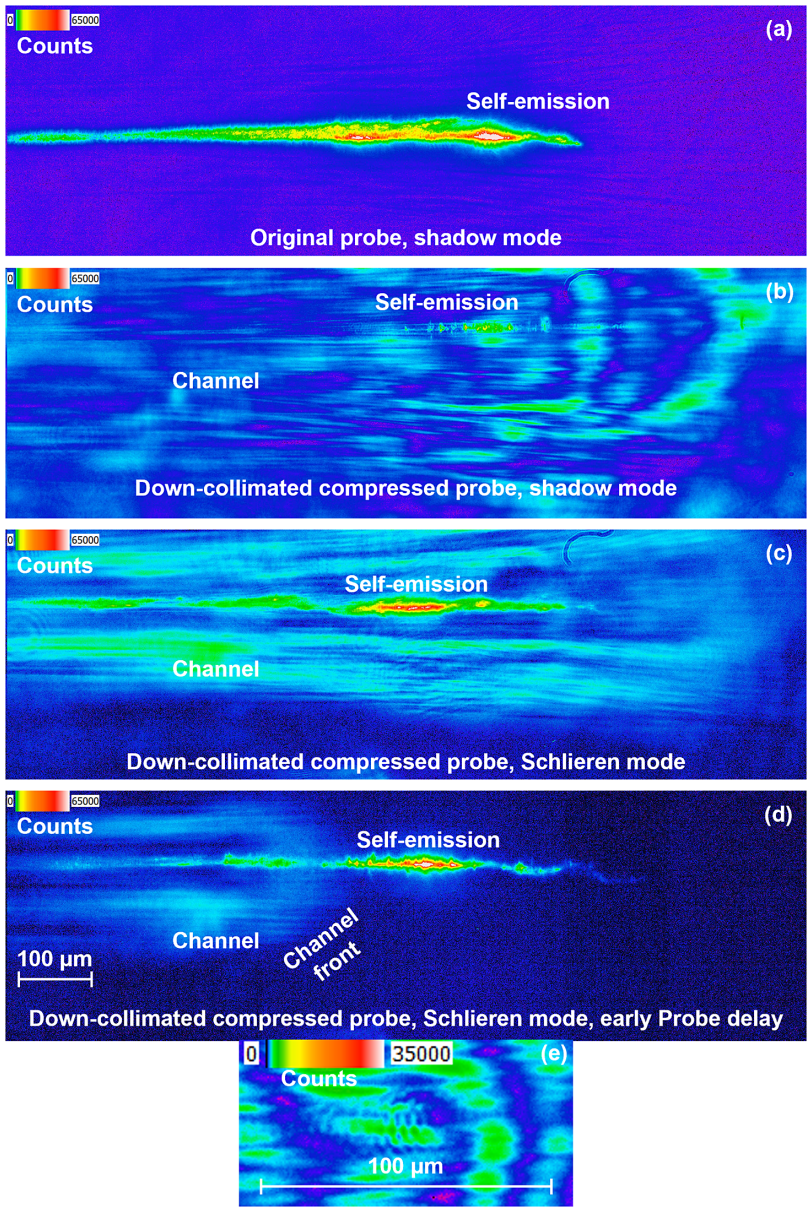

Figure 6. (a)–(d) Representative examples of images produced by the original and down-collimated compressed probe; magnification 10.2, frame size 1920 × 600 pixels, pixel size 1.1 mm × 0.34 mm. The scale bar shown in (d) is common for (a)–(d). (a) Original probe, shadow mode. (b) Down-collimated compressed probe, shadow mode. (c) Down-collimated compressed probe, Schlieren mode. (d) Down-collimated compressed probe, Schlieren mode at an early probe delay. (e) A representative example of fine fringes observed by the compressed probe; note the difference in scale compared to (a)–(d).

near-field profile was sufficiently uniform to produce high-quality images. In particular, we got rather uniformly illuminated images in the shadow mode. Further, the Schlieren data show that, in the case of early probe delay, such as in Figure 6(d), there was no signal before (on the right-hand side of) the main channel front. This indicates that the probe wavefront quality was sufficiently high. If there were distortions, we would have seen them as an intensity pattern in the plasma-free Schlieren image. The spatial resolution estimated from the smallest self-emission spots was 1.4 µm × 1.7 µm.

Using the compressed probe with various plasma density and main pulse energy conditions, we started to see fine fringes with periods from 7 down to approximately 4 µm, with the fringe periods approximately the same as the expected plasma wavelength. The fringe visibility tended to decrease at shorter periods, indicating that we indeed saw these fringes at the limit of the probe duration (we note that the fringe visibility does not turn to zero abruptly; rather, it decreases when the fringe period becomes short compared to the probe length). A representative example is shown in Figure 6(e). These fringes were not observed during many days with the 50 fs probe. Scanning the probe delay with peak plasma density of approximately 9×10^{21} cm^{-3}, we found the velocity of the fringes, $0.87 \times c$. This velocity corresponded to the group velocity of the red-shifted

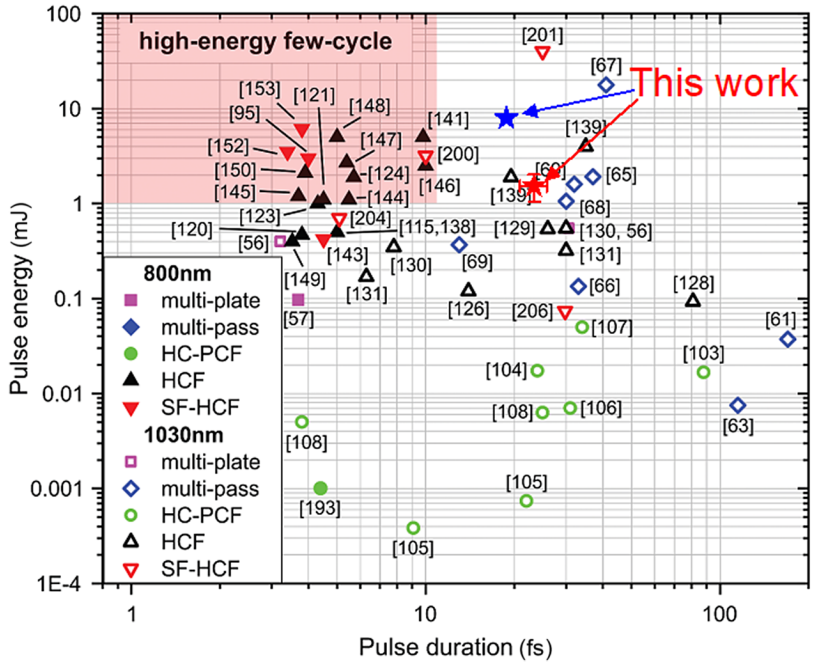

Figure 7. Comparison with other works. Our average BA1×2 data and best BA2×1 data are shown with the red and blue stars, respectively. The figure with other data is reprinted with permission from Ref. [21].

main pulse. These properties correspond to the wakewave, although we note that in our regime of relatively high density (2×10^{19} up to 10^{20} cm^{-3}) and high intensity ($> 10^{20}$ W/cm^2 after self-focusing) where there are other singularities as well.

Comparison of our results on the (pulse duration, pulse energy) plane with other works taken from Ref. [21] is shown in Figure 7.

4. Discussion

The optimum probe pulse compression depends on the laser energy, total nonlinear plate thickness and number of reflections of the chirped mirrors. We estimated the spot-averaged B-integral values to be from 3 to 6 for the PA mode and from 10 to 20 for the BA1×2 mode. These ranges arise from the shot-to-shot probe energy fluctuations. For higher-energy modes, the B-integral values were correspondingly higher; however, self-focusing in the earlier-positioned FS plates could affect the B-integral accumulation in the following plates. In our case in the lowest-energy PA mode the probe phase exhibited some negative chirp (Figure 2(a)) and the optimum was in the BA1×2 mode (Figure 3(b)) with the probe pulse energy of approximately 2 mJ and main pulse energy of 1.3 J. These specific values do not represent a method limitation, but were rather determined by the specific choice of our setup parameters. To shift the optimum to higher-energy modes, the number of reflections should be increased or the number of FS plates reduced. These operations were not motorized in our setup and therefore could not be performed within one experimental day, requiring the target chamber venting and opening.

Returning to the potential problems formulated in the Section 1, our experiments demonstrated the following.

Reaching sufficient probe beam peak intensity for efficient SPM in thin plates. The initial probe peak intensity is indeed too low for efficient SPM. The peak intensity can be increased by probe down-collimation, which is also advantageous as it greatly increases the probe-to-self-emission intensity ratio (Figure 6).

Shot-to-shot peak intensity variations leading to compressed probe duration fluctuations. The probe duration fluctuates significantly shot-to-shot (Figures 3 and 4). We note that a similar problem would happen in a fiber-based setup. A possible solution could be the pick-off mirror not being at the very beam edge, or a mirror with a hole near the beam center for probe pulse extraction.

Compressed probe duration dependence on the main pulse energy. The probe is compressed even when the main pulse energy is changed more than five times, which is a practical limit considering optics damage. The minimum probe duration is approximately 18 fs in almost all laser modes. However, the average compression factor depends on the energy (Figure 3). With a single setup, the energy can be changed by a factor of approximately 1.5 either side of the optimum; for a larger energy variation, an in-vacuum motorized probe attenuator would be desirable. At the optimum energy, the compressed probe duration fluctuations are larger than that of the main pulse; in our case, the compressed

probe duration fluctuated by approximately 9% with some occasional outliers, while the main pulse duration was stable within approximately 2% (Figure 4(a)).

Potential degradation of the probe pulse near-field pattern. The down-collimated compressed probe pulse retains its high quality.

Typically short experimental beam times of high-power user facilities. It is possible to implement the CafCA probe pulse post-compression during a few-week experimental campaign. However, it would be advantageous to implement it as a part of the experimental facility, which would allow its better optimization: in our case, based on the FWHM values of the transform limited pulses that would give an additional compression by a factor of up to 1.5−2. Also, that would allow additional motorizations, for example, the independent insertion of FS plates.

5. Conclusion

In conclusion, we demonstrated experimentally a compact in-vacuum setup for down-collimation of a low peak intensity probe laser pulse and compression of its duration using the CafCA in the optimum regime from approximately 50 down to 24 ± 5 fs (mean $\pm$ standard deviation FWHM value), 23 ± 2 fs (most frequent FWHM value $\pm$ standard deviation without outliers) and 18 fs (the shortest FWHM value), while keeping the pulse synchronized in space and time with the driving laser pulse. Compression from approximately 50 to 23 ± 2 fs reduced the motion blur from approximately 15 down to 6.9 ± 0.6 μm, while for the shortest pulses down to $c \times 18$ fs ≈ 5.4 μm, which already allows one to study density micro-structures in relativistic plasma experiments. We characterized the shot-to-shot fluctuations and measured dependence of the compressed probe pulse parameters on the laser energy while keeping the probe compression setup unchanged; in non-optimum regimes, such as higher-than-optimum pulse energies, we observed larger duration fluctuations. We showed that the down-compression allowed efficient SPM and increased the probe-to-self-emission brightness ratio, while not leading to probe image quality degradation.

Supplementary material

The supplementary material for this article can be found at http://doi.org/10.1017/hpl.2024.29.

Acknowledgments

We thank the J-KAREN-P laser team and acknowledge discussions with Drs. Daniel Symes, Alexander Kotov, Alexander Soloviev, Vladimir Pervak, Michiaki Mori and László Veisz. This work was supported by the projects 'Advanced research using high-intensity photons and particles' (CZ.02.1.01/0.0/0.0/16_019/0000789) from the European Regional Development Fund and a Strategic Grant by the QST President: IRI, and JSPS Kakenhi JP19H00669, JP19KK0355, JP21H01103, and JP23H01151. Gabriele Grittani's work was also supported by the NSF and Czech Science Foundation (NSF-GACR collaborative Grant No. 2206059 and Czech Science Foundation Grant No. 22-42963L).

References

1. N. H. Matlis, S. Reed, S. S. Bulanov, V. Chvykov, G. Kalintchenko, T. Matsuoka, P. Rousseau, V. Yanovsky, A. Maksimchuk, S. Kalmykov, G. Shvets, and M. C. Downer, Nat. Phys. **2**, 749 (2006).
2. A. Buck, M. Nicolai, K. Schmid, C. M. S. Sears, A. Sävert, J. M. Mikhailova, F. Krausz, M. C. Kaluza, and L. Veisz, Nat. Phys. **7**, 543 (2011).
3. M. F. Gilljohann, H. Ding, A. Döpp, J. Götzfried, S. Schindler, G. Schilling, S. Corde, A. Debus, T. Heinemann, B. Hidding, S. M. Hooker, A. Irman, O. Kononenko, T. Kurz, A. Martinez de la Ossa, U. Schramm, and S. Karsch, Phys. Rev. X **9**, 011046 (2019).
4. A. Sävert, S. P. D. Mangles, M. Schnell, E. Siminos, J. M. Cole, M. Leier, M. Reuter, M. B. Schwab, M. Möller, K. Poder, O. Jäckel, G. G. Paulus, C. Spielmann, S. Skupin, Z. Najmudin, and M. C. Kaluza, Phys. Rev. Lett. **115**, 055002 (2015).
5. J. Xu, A. Buck, S.-W. Chou, K. Schmid, B. Shen, T. Tajima, M. C. Kaluza, and L. Veisz, Phys. Plasmas **24**, 083106 (2017).
6. M. C. Kaluza, H.-P. Schlenvoigt, S. P. D. Mangles, A. G. R. Thomas, A. E. Dangor, H. Schwoerer, W. B. Mori, Z. Najmudin, and K. M. Krushelnick, Phys. Rev. Lett. **105**, 115002 (2010).
7. M. C. Downer, R. Zgadzaj, A. Debus, U. Schramm, and M. C. Kaluza, Rev. Mod. Phys. **90**, 035002 (2018).
8. S. V. Bulanov, T. Z. Esirkepov, M. Kando, J. K. Koga, A. S. Pirozhkov, T. Nakamura, S. S. Bulanov, C. B. Schroeder, E. Esarey, F. Califano, and F. Pegoraro, Phys. Plasmas **19**, 113102 (2012).
9. S. V. Bulanov, T. Esirkepov, and T. Tajima, Phys. Rev. Lett. **91**, 085001 (2003).
10. M. Kando, Y. Fukuda, A. S. Pirozhkov, J. Ma, I. Daito, L.-M. Chen, T. Z. Esirkepov, K. Ogura, T. Homma, Y. Hayashi, H. Kotaki, A. Sagisaka, M. Mori, J. K. Koga, H. Daido, S. V. Bulanov, T. Kimura, Y. Kato, and T. Tajima, Phys. Rev. Lett. **99**, 135001 (2007).
11. A. S. Pirozhkov, J. Ma, M. Kando, T. Z. Esirkepov, Y. Fukuda, L.-M. Chen, I. Daito, K. Ogura, T. Homma, Y. Hayashi, H. Kotaki, A. Sagisaka, M. Mori, J. K. Koga, T. Kawachi, H. Daido, S. V. Bulanov, T. Kimura, Y. Kato, and T. Tajima, Phys. Plasmas **14**, 123106 (2007).
12. M. Kando, A. S. Pirozhkov, K. Kawase, T. Z. Esirkepov, Y. Fukuda, H. Kiriyama, H. Okada, I. Daito, T. Kameshima, Y. Hayashi, H. Kotaki, M. Mori, J. K. Koga, H. Daido, A. Y. Faenov, T. Pikuz, J. Ma, L.-M. Chen, E. N. Ragozin, T. Kawachi, Y. Kato, T. Tajima, and S. V. Bulanov, Phys. Rev. Lett. **103**, 235003 (2009).
13. A. S. Pirozhkov, T. Z. Esirkepov, T. A. Pikuz, A. Y. Faenov, K. Ogura, Y. Hayashi, H. Kotaki, E. N. Ragozin, D. Neely, H. Kiriyama, J. K. Koga, Y. Fukuda, A. Sagisaka, M. Nishikino,

T. Imazono, N. Hasegawa, T. Kawachi, P. R. Bolton, H. Daido, Y. Kato, K. Kondo, S. V. Bulnov, and M. Kando, Sci. Rep. **7**, 17968 (2017).
14. A. S. Pirozhkov, M. Kando, T. Z. Esirkepov, P. Gallegos, H. Ahmed, E. N. Ragozin, A. Y. Faenov, T. A. Pikuz, T. Kawachi, A. Sagisaka, J. K. Koga, M. Coury, J. Green, P. Foster, C. Brenner, B. Dromey, D. R. Symes, M. Mori, K. Kawase, T. Kameshima, Y. Fukuda, L. Chen, I. Daito, K. Ogura, Y. Hayashi, H. Kotaki, H. Kiriyama, H. Okada, N. Nishimori, T. Imazono, K. Kondo, T. Kimura, T. Tajima, H. Daido, P. Rajeev, P. McKenna, M. Borghesi, D. Neely, Y. Kato, and S. V. Bulanov, Phys. Rev. Lett. **108**, 135004 (2012).
15. A. S. Pirozhkov, M. Kando, T. Z. Esirkepov, P. Gallegos, H. Ahmed, E. N. Ragozin, A. Y. Faenov, T. A. Pikuz, T. Kawachi, A. Sagisaka, J. K. Koga, M. Coury, J. Green, P. Foster, C. Brenner, B. Dromey, D. R. Symes, M. Mori, K. Kawase, T. Kameshima, Y. Fukuda, L. Chen, I. Daito, K. Ogura, Y. Hayashi, H. Kotaki, H. Kiriyama, H. Okada, N. Nishimori, T. Imazono, K. Kondo, T. Kimura, T. Tajima, H. Daido, P. Rajeev, P. McKenna, M. Borghesi, D. Neely, Y. Kato, and S. V. Bulanov, New J. Phys. **16**, 093003 (2014).
16. A. Pirozhkov, T. Esirkepov, T. Pikuz, A. Faenov, A. Sagisaka, K. Ogura, Y. Hayashi, H. Kotaki, E. Ragozin, D. Neely, J. Koga, Y. Fukuda, M. Nishikino, T. Imazono, N. Hasegawa, T. Kawachi, H. Daido, Y. Kato, S. Bulanov, K. Kondo, H. Kiriyama, and M. Kando, QuBS **2**, 7 (2018).
17. T. Pikuz, A. Faenov, A. Pirozhkov, A. Astapov, G. Klushin, S. Pikuz Jr., N. Nagorskiy, S. Magnitskiy, T. Esirkepov, J. Koga, T. Nakamura, S. Bulanov, Y. Fukuda, Y. Hayashi, H. Kotaki, Y. Kato, and M. Kando, Phys. Status Solidi C **9**, 2331 (2012).
18. A. Sagisaka, K. Ogura, T. Z. Esirkepov, D. Neely, T. A. Pikuz, J. K. Koga, Y. Fukuda, H. Kotaki, Y. Hayashi, B. Gonzalez-Izquierdo, K. Huang, S. V. Bulanov, H. Kiriyama, K. Kondo, T. Kawachi, M. Kando, and A. S. Pirozhkov, High Energy Density Phys. **36**, 100751 (2020).
19. T. Z. Esirkepov, J. Mu, Y. Gu, T. M. Jeong, P. Valenta, O. Klimo, J. K. Koga, M. Kando, D. Neely, G. Korn, S. V. Bulanov, and A. S. Pirozhkov, Phys. Plasmas **27**, 052103 (2020).
20. R. A. Fisher, P. L. Kelley, and T. K. Gustafson, Appl. Phys. Lett. **14**, 140 (1969).
21. T. Nagy, P. Simon, and L. Veisz, Adv. Phys. X **6**, 1845795 (2020).
22. R. Szipöcs, C. Spielmann, F. Krausz, and K. Ferencz, Opt. Lett. **19**, 201 (1994).
23. R. Szipöcs and A. Köhazi-Kis, Appl. Phys. B Lasers Opt. **65**, 115 (1997).
24. N. Matuschek, F. X. Kartner, and U. Keller, IEEE J. Select. Topics Quantum Electron. **4**, 197 (1998).
25. M. B. Schwab, A. Sävert, O. Jäckel, J. Polz, M. Schnell, T. Rinck, L. Veisz, M. Möller, P. Hansinger, G. G. Paulus, and M. C. Kaluza, Appl. Phys. Lett. **103**, 191118 (2013).
26. D. R. Symes, E. J. Divall, and U. Wegner, "Operation of the Astra TA2 hollow fibre pulse compressor with increased pump energy," CLF Annual Report 2008/2009 S7 229 (2009).
27. V. Ginzburg, I. Yakovlev, A. Kochetkov, A. Kuzmin, S. Mironov, I. Shaikin, A. Shaykin, and E. Khazanov, Opt. Express **29**, 28297 (2021).
28. P.-G. Bleotu, J. Wheeler, D. Papadopoulos, M. Chabanis, J. Prudent, M. Frotin, L. Martin, N. Lebas, A. Freneaux, A. Beluze, F. Mathieu, P. Audebert, D. Ursescu, J. Fuchs, and G. Mourou, High Power Laser Sci. Eng. **10**, e9 (2022).
29. S. Y. Mironov, J. Wheeler, R. Gonin, G. Cojocaru, R. Ungureanu, R. Banici, M. Serbanescu, R. Dabu, G. Mourou, and E. A. Khazanov, Quantum Electron. **47**, 173 (2017).
30. J. Wheeler, G.P. Bleotu, A. Naziru, R. Fabbri, M. Masruri, R. Secareanu, D. M. Farinella, G. Cojocaru, R. Ungureanu, E. Baynard, J. Demailly, M. Pittman, R. Dabu, I. Dancus, D. Ursescu, D. Ros, T. Tajima, and G. Mourou, Photonics **9**, 715 (2022).
31. G. Mourou, S. Mironov, E. Khazanov, and A. Sergeev, Eur. Phys. J. Spec. Top. **223**, 1181 (2014).
32. J. I. Kim, Y. G. Kim, J. M. Yang, J. W. Yoon, J. H. Sung, S. K. Lee, and C. H. Nam, Opt. Express **30**, 8734 (2022).
33. E. A. Khazanov, S. Y. Mironov, and G. Mourou, Phys.-Usp. **62**, 1096 (2019).
34. A. V. Kotov, T. Z. Esirkepov, A. A. Soloviev, A. Sagisaka, K. Ogura, A. Bierwage, M. Kando, H. Kiriyama, M. V. Starodubtsev, E. A. Khazanov, S. Y. Mironov, and A. S. Pirozhkov, J. Inst. **17**, P07035 (2022).
35. M. B. Schwab, E. Siminos, T. Heinemann, D. Ullmann, F. Karbstein, S. Kuschel, A. Sävert, M. Yeung, D. Hollatz, A. Seidel, J. Cole, S. P. D. Mangles, B. Hidding, M. Zepf, S. Skupin, and M. C. Kaluza, Phys. Rev. Accel. Beams **23**, 032801 (2020).
36. T. Nagy, M. Kretschmar, M. J. J. Vrakking, and A. Rouzée, Opt. Lett. **45**, 3313 (2020)
37. A. S. Pirozhkov, Y. Fukuda, M. Nishiuchi, H. Kiriyama, A. Sagisaka, K. Ogura, M. Mori, M. Kishimoto, H. Sakaki, N. P. Dover, K. Kondo, N. Nakanii, K. Huang, M. Kanasaki, K. Kondo, and M. Kando, Opt. Express **25**, 20486 (2017).
38. H. Kiriyama, Y. Miyasaka, A. Kon, M. Nishiuchi, A. Sagisaka, H. Sasao, A. S. Pirozhkov, Y. Fukuda, K. Ogura, K. Kondo, N. P. Dover, and M. Kando, High Pow Laser Sci. Eng. **9**, e62 (2021).
39. A. Moulet, S. Grabielle, C. Cornaggia, N. Forget, and T. Oksenhendler, Opt. Lett. **35**, 3856 (2010).
40. S. Lorenz, G. Grittani, E. Chacon-Golcher, C. M. Lazzarini, J. Limpouch, F. Nawaz, M. Nevrkla, L. Vilanova, and T. Levato, Matter Radiat. Extremes **4**, 015401 (2019).
41. C. M. Lazzarini, G. M. Grittani, P. Valenta, I. Zymak, R. Antipenkov, U. Chaulagain, L. V. N. Goncalves, A. Grenfell, M. Lamac, S. Lorenz, M. Nevrkla, V. Sobr, A. Spacek, W. Szuba, P. Bakule, G. Korn, and S. V. Bulanov, Phys. Plasmas **31**, 030703 (2024).
42. L. M. Chen, W. C. Yan, D. Z. Li, Z. D. Hu, L. Zhang, W. M. Wang, N. Hafz, J. Y. Mao, K. Huang, Y. Ma, J. R. Zhao, J. L. Ma, Y. T. Li, X. Lu, Z. M. Sheng, Z. Y. Wei, J. Gao, and J. Zhang, Sci. Rep. **3**, 1912 (2013).
43. Z. Bor, J. Mod. Opt. **35**, 1907 (1988).
44. Z. Bor, Opt. Lett. **14**, 119 (1989).
45. H. Kiriyama, A. S. Pirozhkov, M. Nishiuchi, Y. Fukuda, A. Sagisaka, A. Kon, Y. Miyasaka, K. Ogura, N. P. Dover, K. Kondo, H. Sakaki, J. K. Koga, T. Z. Esirkepov, K. Huang, N. Nakanii, M. Kando, K. Kondo, S. Bock, T. Ziegler, T. Püschel, K. Zeil, and U. Schramm, Crystals **10**, 783 (2020).